Microcracks in CVD diamond produced by scaife polishing

E. Saho [a,b,*], S. Hindmarsh [c], A.M. Sanchez [a], F. Birks [d], J.R. Kermode [d], M.W. Dale [e], D. Fisher [e], R. Beanland [a,**]

[a] *Department of Physics, University of Warwick, Coventry CV4 7AL, UK*
[b] *Centre for Doctoral Training in Diamond Science and Technology, University of Warwick, Coventry CV4 7AL, UK*
[c] *Electron Microscopy RTP, University of Warwick, Coventry CV4 7AL, UK*
[d] *Warwick Centre for Predictive Modelling, School of Engineering, University of Warwick, Coventry CV4 7AL, UK*
[e] *De Beers Group IGNITE™, Incubation Research, Maidenhead SL6 6JW, UK*

ARTICLE INFO

ABSTRACT

We investigate sub-surface damage in a CVD diamond, polished on a (110) plane using the traditional scaife method. The damage lies in tracks that consist of microcracks lying perpendicular to the polishing direction. These cracks have an irregular spacing and are comprised mainly of {111} facets. Their geometry is consistent with a modified Hertzian fracture, caused by a stick-slip movement of relatively large (micron-sized) diamond particles on the scaife. The interior surface of the cracks shows a 1×1 CH3 surface reconstruction, consistent with a high hydrogen overpressure that results from ingress of hydrocarbons in the polishing lubricant and a relatively low temperature process. The crack edge is ragged, and voids with sizes of a few nm are found up to hundreds of nm from the crack front, particularly where the crack ends at the polished surface. We propose that these features are evidence of significant healing of the cracks once the applied stress is removed. Luminescence at the crack tips is seen, presumably due to impurities trapped in these voids, which quenches with electron irradiation at 10 keV.

1. Introduction

Mechanical polishing of diamond gemstones, using fine diamond dust on a fast-rotating iron or steel wheel, was already developed as a technology by the 1500s [1], and has remained essentially unchanged to the present day. The method, which allows the hardest known material to be shaped and polished, attracted scientific interest over the last century [2–4], in particular the puzzling and large anisotropy in material removal rate depending both on the crystal facet and the direction of movement of the wheel ('scaife') surface relative to the facet [3,5]. The most obvious model of material removal for such a hard and brittle material, i.e. cleavage on a finer and finer scale [5,6], is appropriate for coarse shaping. However, it cannot satisfactorily explain the anisotropy in friction that accompanies the 'hard' and 'soft' polishing directions; for example in polishing a (110) facet of a single-crystal stone, the soft [001] direction may have a rate of material removal a thousand times larger, and a friction coefficient ten times larger, than the hard [1$\bar{1}$0] direction [3,7–9]. Furthermore, microscopic analysis of the surface of

both polished single crystals, and the diamond fragments embedded in the scaife surface, showed them to be macroscopically flat, with nano-scale grooves along the polishing direction [9–11]. Such a surface morphology is clearly not produced by cleavage, while plastic deformation below ~800 °C does not take place in diamond [12]. This observation led to the proposal that intimate contact of a diamond particle sliding on the surface under high pressure produces a change in the outermost atomic layers, converting sp^3-bonded carbon in the diamond to sp^2-bonded graphitic or amorphous material that is readily removed [7,8,13]. Atomistic modelling not only confirmed this hypothesis [14–16], but also reproduced the anisotropy of both removal rate and friction.

These studies have firmly established the principles of traditional diamond polishing methods. It is still widely used, alongside other more sophisticated methods such as plasma etching and laser ablation, with applications in a wide range of areas (see e.g. [4,17–20] for reviews). Modern scaife polishing uses a cast-iron wheel 300 mm in diameter and 20 mm thick [5,7,21] loaded with diamond powder and lubricant (e.g.

---

mineral oil) rotating at ~3000 rpm, and an applied pressure typically in the 10 MPa range (i.e. 1 kg on a surface area of 1 mm²). Nevertheless, preparing – and maintaining – the quality of the scaife surface ('boarting') [2,3,11] and using it to polish a single crystal remains a skilled craft. Removal of all damage can be difficult, particularly when relying on methods that image only surface roughness and do not reveal sub-surface damage [22]. Cleavage of material from the crystal no longer occurs once a planar surface is established, but the crystal may still be susceptible to the generation of cracks produced by large compressive stresses. (Indeed, Hertzian fracture [23] induced by ball-shaped diamond indenters is one of the principal methods used to measure the strength of diamond [24–27].) Such stresses can be produced when only a few small diamond particles in the scaife are in contact with the surface, multiplying the applied stress by several orders of magnitude. In Hertzian fracture, the highest stress is found just outside the contact area of the indenter and the crack forms at the surface there, expanding as a cone that spreads out below the surface from the indentation site. When produced by a sliding indenter with high friction, the stress is increased at the trailing edge and decreased at the leading edge of contact. This produces a tilted cone, or a single arc-shaped crack at the trailing edge of the indenter. Repeated fracture, occurring as the indenter travels across the surface, produces multiple microcracks lying perpendicular to the direction of sliding [28,29]. In scaife diamond polishing, these damage tracks are often the most stubborn problem, while also being difficult to detect.

Despite the attention given to the polishing process, there have been no in-depth investigations of microcrack damage produced during scaife polishing. Here, we address this omission, using cathodoluminescence (CL) together with focused ion beam (FIB) specimen preparation and transmission electron microscopy (TEM) to investigate damage tracks in a CVD-grown diamond polished on a (110) plane.

2. Results

Sub-surface scaife damage is not readily visible either by optical investigation of in SEM images; the surface appears smooth and featureless. However, it is readily visible in CL [30]. Panchromatic cathodoluminescence microscopy of the scaife-polished (110) plane of our CVD diamond with a primary electron beam energy of 10 keV shows diffuse background luminescence, punctuated by bright spots associated with threading dislocations. As shown in Fig. 1, residual polishing damage is visible as parallel sets of dark arcs, or short lines along [$\bar{1}$10], that form damage tracks. All arcs bend in the same direction along the track, towards the top of Fig. 1 and, as will be shown below, these are microcracks in the diamond surface. By comparison with similar damage tracks in the literature [28,29], the diamond particles in the scaife which caused them moved from top to bottom of the image, i.e. along [00$\bar{1}$]. In most cases the arcs in a track all have the same width (typically between 0.5 and 3 µm), suggesting a common origin, i.e. a single diamond particle in the scaife. The spacing of microcracks is not regular, for example in the track marked A. Some tracks (e.g. that to the left of A) have much finer spacing, but it is not clear whether these are a single track or two or more overlapping tracks. It is also noticeable that tracks can change their morphology over lengths of tens of micrometres. These variations are consistent with a chaotic process such as a stick-slip interaction, rather than some oscillation with a well-defined frequency. The lines appear dark against the background luminescence, indicating that they act as non-radiative recombination centres. However, many of the arcs in Fig. 1 also have a spot of bright luminescence at one end, and occasionally both ends. Interestingly, this luminescence at the ends of the arcs quenches rapidly under electron irradiation (Supplementary Fig. SI1), typically disappearing in a few tens of seconds, preventing the capture of a CL spectrum. Thus, this damage has quite complex characteristics with both radiative and non-radiative character.

Following CL, FIB-SEM was used to prepare a plan-view lamella for examination by TEM. A lamella thickness of 1.3 µm was used to capture the full depth of the cracks and while this is rather thick for TEM, good images could be obtained using anomalous transmission in 2-beam diffraction conditions, as can be seen in Fig. 2. Here, it is apparent that the arc-shaped microcracks have a complicated morphology. Each one has a width of almost 1 µm in projection at its centre, indicating that it is inclined to the point of view, i.e. the crack intersects the top surface
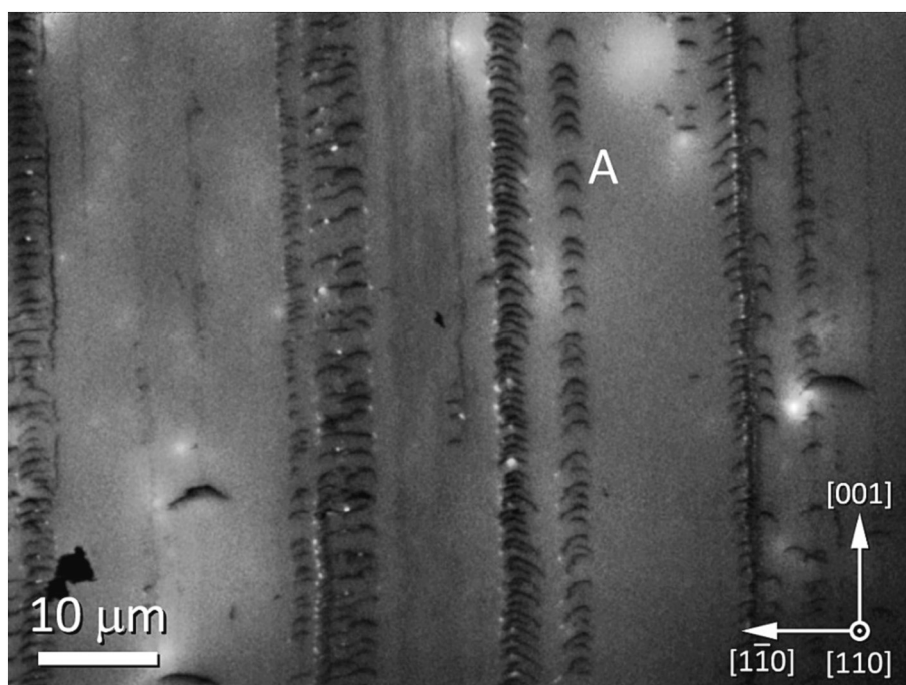

Fig. 1. Panchromatic CL image of damage tracks on a CVD diamond (110) polished surface. Each track consists of an array of microcracks, dark against the background luminescence, lying perpendicular to the track direction. Many microcracks show luminescence as a small bright spot at their tip. Spacings of the microcracks in track A are shown in Fig. 5.
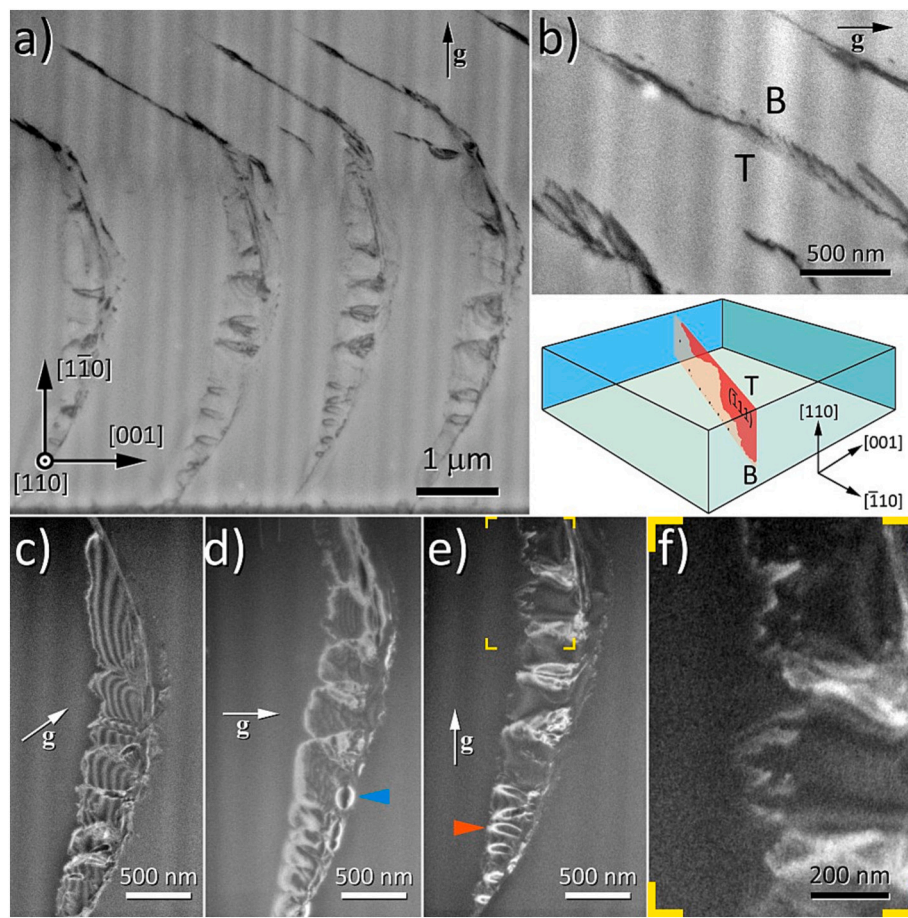
Fig. 2. a) Plan view bright field TEM image of four arc-shaped microcracks in a clatter track. The top ends of the cracks were luminescent. b) Higher magnification bright field image of the luminescent end of a microcrack, seen in projection. The schematic below shows the three-dimensional geometry. c-e) Dark field images of microcracks using g = −111, 004 and 220 diffraction conditions respectively. Dislocation loops are indicated by arrowheads. N.B. (d) and (e) are the same microcrack, (c) is not. f) Enlargement of the region marked in (e) showing the ragged lower edge of the microcrack.
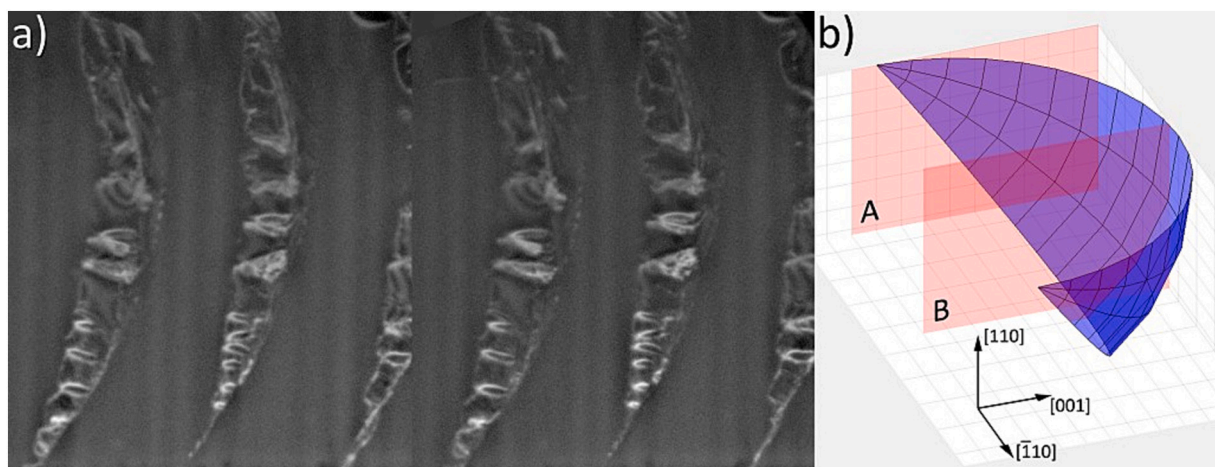

Fig. 3. a) [110] plan view TEM stereo pair of microcracks (dark field, g = 2$\bar{2}$0). b) Idealised microcrack geometry, and location of subsequent FIB-SEM cross sections A and B.

Panel a shows a stereo pair, allowing the three-dimensional geometry of the microcracks to be determined (see also the animation SI2). This is shown, idealised as a section of a spherical surface, in panel b. In reality, the crack is quite facetted, with large steps appearing as white triangular regions in Fig. 4a, and the ends of the crack lying on {111} planes. After imaging in plan-view geometry, two FIB-lift out cross sections were taken from the specimen A) at the luminescent end and B) through the centre of the microcracks, as indicated in Panel b.

on the right, with the lower edge inside the lamella on the left. The projected width tapers towards the edges of the microcrack, and in Fig. 2a the luminescent ends of the cracks – closest to the top of the image – are straight and thin, indicating that the cracks here are flat ($\bar{1}11$) planes, and lie edge-on. Higher magnification images (Fig. 2b) show the structure of these flat cracks. Here, the sample is tilted so that the plane is seen slightly in projection, as a band of contrast. The intersection of the crack with the top surface is at the lower edge (marked T), while a line of dots is visible deeper in the material (marked B). The morphology is illustrated in the accompanying schematic, showing the three-dimensional geometry with the ($\bar{1}11$) plane in orange, and the crack in red. The lower edge of the crack lies between the top surface and the line of dots, visible in the TEM image as a dark wavy line of contrast.

Fig. 2c-e shows the central part of the microcracks under different two-beam dark field imaging conditions. Fig. 2c, using g = $\bar{1}11$, gives strong moiré fringes where the crack is open, while Fig. 2d, g = 004, shows dislocation loops with Burgers vector components parallel to [001] at the top surface (e.g. blue arrowhead). Fig. 2e, g = $2\bar{2}0$, shows dislocation loops with Burgers vector components perpendicular to the crack plane (e.g. orange arrowhead). There are only a few dislocations associated with each microcrack, and none at the crack tip, which is typical behaviour for diamond [31]. Interestingly, in all these images it is apparent that the crack has a ragged edge. This is shown in the enlarged image Fig. 2f, which shows undulations and incursions in the crack edge of 200 nm or more. This geometry is clearly incompatible with the notion of crack propagation by the motion of kinks along a relatively straight crack edge [32], and therefore shows some change to the crack that occurred sometime after the initial fracture.

Fig. 4 shows TEM images of two microcrack ends in cross section. The ragged crack edge is quite apparent as well as several spots some distance in front of the crack edge, which appear bright in these dark field images. These are the same features that appear as dark dots in the bright field plan view TEM image of Fig. 2b. They do not appear to be dislocations, and show similar contrast behaviour to the crack; the most plausible explanation of these features is that they are small planar voids. This, together with the uneven edge of the crack, suggests that the crack initially propagated several hundred nm further than its observed position, and healed again, for the most part seamlessly. The bright spots in Fig. 4 are thus small regions where healing was not possible for some reason.

Cross section B, cutting through the centre of a microcrack, is shown in Fig. 5. Fig. 5a is a bright field STEM image, showing very clearly the faceted nature of the crack and its changing habit plane throughout its depth. Also apparent are dislocations at the top surface (but nowhere else). Approx. 500 nm below the surface the crack changes orientation from ($11\bar{1}$) to (111), switching back again roughly 100 nm deeper. At these sharp changes in orientation the crack bifurcates. A dark field ADF-STEM image of the tip of one of these bifurcated crack tips is shown in Fig. 5b, from the area marked by the red square on Fig. 5a. Here, the atomic structure is clearly visible in the bulk of the crystal with atom columns arranged in the familiar 'dumbbell' pairs. Interestingly, at the ($11\bar{1}$) crack surfaces the dumbbell is not visible; the crystal is terminated

by only one bright spot, rather than a pair, i.e. the crack surface is reconstructed. We thus modelled surface reconstructions by seeding and relaxing a (111) diamond surface using the MatSciPy package [33] in which interactions between atoms were described using a machine-learned carbon interatomic potential, built using the atomic cluster expansion formalism [34]. There are three known reconstructions of the diamond {111} surface [35,36]: (i) 1×1 CH3-terminated, with each surface C atom tetrahedrally coordinated to one C atom in the layer below and three H atoms above; (ii) 1×1 CH-terminated, with each surface atom tetrahedrally coordinated to three C atoms in the layer below and one H atom above; and (iii) a 2×1 reconstruction, with no bonded hydrogen. The lower symmetry of the latter presents two possible {110} views. Multislice annular dark field (ADF) STEM simulations of these modelled reconstructions, with the same geometry of the observed crack, are shown on the right of Fig. 5b. Comparison of the experimental image and the simulated structures clearly demonstrates that the observed structure corresponds to the 1×1 CH3 structure.

3. Discussion

It is apparent from the above data that the damage induced by scaife polishing has a complex character. Several aspects are worth discussion, bearing in mind the specific parameters used in polishing this particular stone (see Methods). These are similar to those described by Hird and Field [11], who showed that diamond powder in their boarted scaife surface presented flat surfaces optimised for polishing.

We first consider the microcracks and their morphology. We assume a maximum load of 4 kg on the surface area of 4 mm², i.e. a nominal applied stress of 10 MPa. Hertzian cracks in diamond produced by static indenters of micron-scale dimensions generally require stresses above 50 GPa [26]. (N.B. For a Hertzian cone angle of around 55°, i.e. the angle between the {111} cleavage plane and the (110) surface, and a low coefficient of friction [8] $f < 0.5$, there is essentially no correction to this value resulting from the relative movement of the surface and particle [37]. However, the assumption of low friction may not be valid in this case, as discussed further below.) Such a high stress would be produced if the actual contact area between workpiece and scaife was only 200 µm², for example borne by fifty 2×2 µm diamond fragments. Thus, damage tracks may be expected to form when a scaife is lightly loaded, with only tens of diamond particles per mm².

At first sight, the damage tracks here have a strong resemblance to the damage produced by a sliding ball indenter in brittle materials such as soda glass [29,37], which also appears as a set of arc-shaped cracks. However, a crack forming a Hertzian cone tends to become aligned orthogonally to the most tensile of the principal stresses [24] which, in static indentation, results in a curvature of the crack plane to become more parallel to the surface further from its origin [23,37]. The crack in Fig. 5 does the opposite, curving underneath the initiation of the crack at the surface. This is probably a result of the very high speed of rotation. For a scaife running at 3000 rpm and the diamond workpiece held on the scaife wheel at a radius of 100 mm, the relative velocity of the diamond and scaife is 3.14×10^7 µm s^{-1}, i.e. a distance of 1 µm is passed in a time of only 32 ns. Fig. 6a shows the irregular spacing between microcracks (track A in Fig. 1). The average spacing between cracks is 1.6 µm (52 ns),
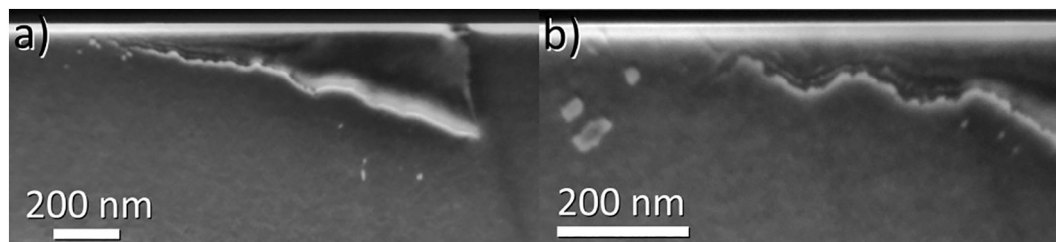

Fig. 4. a) and b) [$\bar{1}10$] Cross section TEM images of the luminescent ends of two microcracks, corresponding to position A in Fig. 3b (dark field, g = 220).
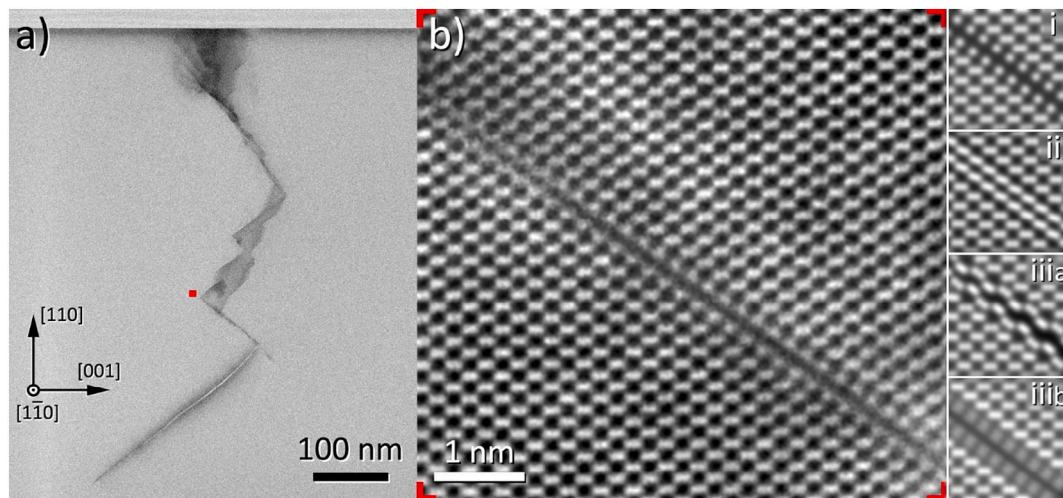
Fig. 5. a) Bright field STEM [1̄10] cross section through the centre of a microcrack (position B in Fig. 3b). The red rectangle marks the location of b), ADF-STEM image of the end of a crack. On the right, multislice simulations of the three different (111) surface reconstructions are compared: (i) C—H3 1 × 1; (ii) C—H 1 × 1; (iiia) 2 × 1 view (a); (iiib) 2 × 1 view (b). In (i) a full relaxation of hydrogen and surface carbon atoms was not performed.
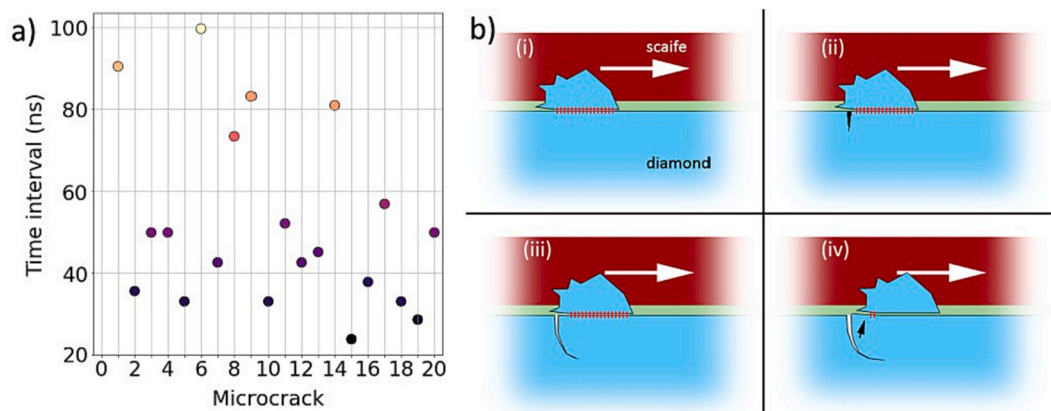

Fig. 6. a) Time interval between microcracks for track A in Fig. 1, assuming a scaife speed of 3000 rpm. b) Proposed stick-slip mechanism of microcrack formation. (i) binding contact of a diamond particle in the scaife and the surface of the workpiece, with carbon-carbon bonds indicated by red lines. (ii) The relative movement of the two surfaces initiates a crack at the trailing edge of the scaife particle. (iii) Propagation of the crack under the scaife particle (iv) opening of the crack produces a small change in surface orientation that aids breaking of carbon-carbon bonds and release of the scaife particle.

but intervals can be as small as 0.75 μm (24 ns) or as large as 3.1 μm (100 ns). While these times are short, the crack velocity in diamond is estimated to be 3000-6000 m/s, i.e. a crack 1 μm deep will form in approximately 0.2 ns, an order of magnitude faster. Nevertheless, in this short time the relative movement of particle and diamond is 6 nm, which may be enough to change the principal stresses as the crack propagates. It is also possible that the crack moves more slowly [38] and develops in multiple stages. We also note that friction coefficients at contact pressures in the range of tens of GPa may be significantly higher than measurements made at lower values [8]. This is also supported by the proposed polishing mechanism since converting the surface layer from sp^3 tetrahedrally bonded atoms to graphitic or amorphous sp^2 carbon relies on 'cold welding' of C—C bonds between the two diamond surfaces [14,16]. A high coefficient of friction increases the stress gradient at the trailing edge of the particle and can lower the stress at which cracking occurs by up to 30 % [37]. Thus, the crack morphology suggests formation by a stick-slip mechanism, as illustrated in Fig. 6b. The interaction begins at (i), where a flat-topped fragment comes into intimate (binding) contact with the surface, producing a large compression and shear strain in the diamond and (ii) opening a crack. The relative movement of particle and surface influences the trajectory of the crack, which follows the arc of maximum tensile stress under the fragment (iii).

Finally (iv), the change in surface angle, which can take place as the crack grows, breaks the close contact, releasing the fragment and leaving a curved crack in the stone.

After crack formation, other processes take place. Given the speed of crack propagation, the newly formed surfaces will initially be in vacuum, and will reconstruct on a timescale of a few picoseconds. Kern et al. [39] noted that models of a pristine diamond {111} surface predict the develops a 2 × 1 π-bonded reconstruction, with chains of dimers along one of the <1̄10> directions on the surface, like that shown in Fig. 5b (iiia, iiib). However, the vacuum will not be maintained for long, and the crack will fill with polishing media (i.e. oil), atmosphere and residual polishing products, if sufficiently small. Below about 900 °C a hydrogen-terminated CH 1 × 1 reconstruction (Fig. 5b ii) is generally considered to be the most energetically favourable structure [36,40], and there is a ready supply of hydrogen in the lubricant. However, as is clear from Fig. 5b the {111} crack surface is not CH terminated, but is in fact CH3 terminated. While recent publications generally only consider 1 × 1 CH-terminated surfaces at lower temperatures, early studies [35,41–43] clearly detect high hydrogen levels on polished diamond surfaces that have not been exposed to temperatures above 450 °C. These studies led to the suggestion that the 1 × 1 CH3 reconstruction is stable at high hydrogen overpressures [44] and Fig. 5 seems to support this proposal.

Our observations also suggest there has been significant crack healing – over several hundred nm from the initial end of the crack. Evidence of crack healing in diamond has recently been observed during in-situ deformation tests of nanocrystalline diamond/amorphous carbon composite material [45–48] and has been documented in HPHT-treated diamond [49], as well as in other materials with pristine surfaces [50]. All these studies were performed in vacuum, whereas in our case the healing upwards from the lower crack tip must take place in competition with ingress of foreign atoms and molecules into the top of the crack; the relative velocities of these two processes are therefore important. When the sliding diamond scaife fragment is released by the polished surface (Fig. 6b), there are no longer stresses acting to hold the crack open, and it may thus close once more if there is nothing preventing it from doing so. At the atomic scale, there are two barriers to seamless healing of the pristine surfaces at the crack tip: a) reversal of any 2×1 surface reconstruction of the crack surfaces, and b) the movement of a kink on the crack edge, which is a thermally activated, reversible process [38]. A full investigation of the possible presence of surface reconstruction in a newly-formed crack is beyond the scope of this work and thus remains to be quantified. For the movement of kinks on the crack front, based on comparisons with results reported for fracture in silicon [38], we estimate that the activation energy for movement of a kink on a (111) crack with a <110> edge in diamond at a stress intensity factor exceeding the Griffith critical value is very low and certainly within the thermal energy available. Nevertheless, it is difficult to estimate the viability and speed of either of these processes. We may also add residual long-range stresses as a third, ultimately limiting, barrier that is responsible for the open cracks visible in Fig. 5a, resulting from snagged protuberances on the stepped and curved crack surface that prevent its closure. The rate of ingress of material into the crack, from processes including surface diffusion and meniscus effects [51] is also difficult to quantify. However, the presence of voids several hundred nm in front of the observed crack edge is strong evidence for significant crack healing, while the ragged edge of the crack is consistent with the inherent instability of diffusion fronts. We speculate that the voids may remain due to contamination of the surface, which prevent seamless healing. From this hypothesis, we might therefore expect that competition between ingress and healing is more important at the lateral ends of the crack, which do not go far below the surface, rather than in its centre where it is deeper, wider and remains open near the surface. This difference in behaviour with crack depth would explain why most voids can be found at the microcrack tips (Fig. 4).

In CL the microcracks appear dark, indicating that they are non-radiative recombination centres. This is consistent with a reconstructed crack surface, although it seems there are no recent simulations of the CH3 1×1 surface that we observe, which could confirm a non-radiative recombination path. The luminescence at the crack tips is probably related to the voids observed there and their decay under irradiation by a 10 keV electron beam indicates a relatively unstable structure. While this electron beam energy is insufficient to damage diamond or most solid materials, it is more than sufficient to destabilise many hydrocarbon molecules. This observation is therefore consistent with the proposal that these voids contain impurities from the polishing media.

4. Summary and conclusions

We have examined sub-surface damage tracks in a high purity CVD diamond scaife-polished on a (110) plane using cathodoluminescence and transmission electron microscopy. They consist of sets of microcracks with an average orientation that is perpendicular to the polishing direction. They have irregular spacing and are consistent with a modified Hertzian fracture, caused by a stick-slip movement of relatively large (micron-sized) diamond particles on the scaife. The cracks curve under the surface but predominantly lie on {111} facets. The interior surface of the cracks shows a 1×1 CH3 surface reconstruction,

consistent with a high hydrogen overpressure that results from ingress of hydrocarbons in the polishing lubricant and a relatively low temperature process, since a CH 1×1 reconstruction is stabilised by temperatures above 450 °C [35]. The crack edge is ragged, and voids with sizes of a few nm are found up to hundreds of nm from the crack front, particularly where the crack ends at the polished surface. We propose that these features are evidence of significant healing of the cracks once the applied stress is removed. Luminescence at the crack tips is seen, presumably due to impurities trapped in these voids, which quenches with electron irradiation at 10 keV.

5. Methods

A 0.23 ct CVD-grown type IIa diamond was used in this work. A 2 mm × 2 mm (110) surface was planarized and polished along the 'soft' [001] direction using a diamond-loaded scaife wheel, 300 mm in diameter and 20 mm thick, rotating at 3000 rpm, loaded with diamond powder and lubricated with a small amount of hydrotreated heavy napthenic distillate (CAS# 64742-52-5). The wheel was conditioned using a boart stone. The applied pressure to the workpiece was between 1 and 4 kg. Typical images of the diamond powder, as supplied prior to application on the scaife, are given in supplementary Figure SI3.

Surface imaging and CL was performed on a Zeiss SUPRA 55VP field emission scanning electron microscope (SEM), equipped with a parabolic mirror that reflects emitted light into a Horiba CLUE CL spectrometer. Panchromatic imaging was performed using a primary beam energy of 10 keV at room temperature and high beam current (beam-limiting aperture 120 μm), using a fast photomultiplier tube (PMT) without filters. A thin (~5 nm) glassy carbon layer was evaporated on the surface prior to SEM imaging to mitigate charging by the electron beam.

Simultaneously acquired secondary electron and CL images were used to identify a region containing damage tracks suitable for further investigation. Lift-out specimens for TEM were prepared using a Tescan Amber FIB-SEM using Ga$^+$ ions at 30 kV, with a 5 kV final stage to reduce surface damage. A large (approximately 10 × 10 μm) and relatively thick (1.3 μm) plan-view lamella was cut from the chosen region, capturing the full thickness of the sub-surface damage. Conventional TEM imaging of this lamella was performed using a JEOL 2100plus HC microscope operating at 200 kV. The sample was then returned to the FIB-SEM and two cross sections were extracted from the lamella cutting through the centre and luminescent end of the microcracks. These lamellae were thinned to approximately 50 nm, allowing high resolution imaging. Atomic resolution scanning TEM (STEM) was performed with an aberration-corrected JEOL ARM200F operating at 200 kV. The incident beam semi-convergence was 22 mrad, giving an electron probe approximately 0.75 Å FWHM with a current of 0.38 pA. Bright field (BF) and annular dark field (ADF) images were obtained using scintillator detectors with radii of 40 mrad and 45–180 mrad respectively.

CRediT authorship contribution statement

E. Saho: Writing – original draft, Visualization, Validation, Project administration, Methodology, Investigation, Formal analysis, Data curation. **S. Hindmarsh:** Investigation. **A.M. Sanchez:** Writing – review & editing, Visualization, Validation, Supervision, Investigation, Formal analysis. **F. Birks:** Writing – review & editing, Software. **J.R. Kermode:** Writing – review & editing, Validation, Software. **M.W. Dale:** Writing – review & editing, Resources, Project administration, Funding acquisition. **D. Fisher:** Writing – review & editing, Resources, Project administration, Funding acquisition. **R. Beanland:** Writing – review & editing, Visualization, Validation, Supervision, Project administration, Funding acquisition, Formal analysis, Conceptualization.

Declaration of competing interest

The authors declare no competing interests.

Data availability

All data are available in the main text or the supplementary information section.

Acknowledgements

Appendix A. Supplementary data

Supplementary data to this article can be found online at https://doi.org/10.1016/j.diamond.2024.111008.

References

[1] B. Cellini, C.R. Ashbee, The Treatises of Benvenuto Cellini on Goldsmithing and Sculpture, 1898th ed., Wellcome Collection, London, 1568. https://wellcomecollection.org/works/tv3pfh6t. (Accessed 14 August 2023).

[2] P. Grodzinski, Diamond Technology - Production Methods for Diamond and Gem Stones, NAG Press, London, 1953.

[3] M. Seal, The abrasion of diamond, Proc. R. Soc. A: Math. Phys. Eng. Sci. 248 (1958) 379–393, https://doi.org/10.1098/rspa.1958.0250.

[4] T. Schuelke, T.A. Grotjohn, Diamond polishing, Diam. Relat. Mater. 32 (2013) 17–26, https://doi.org/10.1016/j.diamond.2012.11.007.

[5] E.M.M. Wilks, J.M. Wilks, The resistance of diamond to abrasion, J. Phys. D. Appl. Phys. 5 (1972) 1902–1928.

[6] M. Tolkowsky, Research on the Abrading, Grinding or polishing of Diamonds, University of London, 1920. https://ethos.bl.uk/OrderDetails.do?did=1&uin=uk.bl.ethos.538936.

[7] S.E. Grillo, J.E. Field, The polishing of diamond, J. Phys. D. Appl. Phys. 30 (1997) 202–209.

[8] S.E. Grillo, J.E. Field, F.M. Van Bouwelen, Diamond polishing: The Dependency of Friction and Wear on Load and Crystal Orientation, 2000.

[9] N. Yang, W. Zong, Z. Li, T. Sun, Wear process of single crystal diamond affected by sliding velocity and contact pressure in mechanical polishing, Diam. Relat. Mater. 58 (2015) 46–53, https://doi.org/10.1016/j.diamond.2015.06.004.

[10] M.S. Couto, W.J.P. Van Enckevort, M. Seal, Friction tracks on diamond surfaces imaged by atomic force microscopy, Diam. Relat. Mater. 6 (1997) 975–982.

[11] J.R. Hird, J.E. Field, Diamond polishing, Proc. R. Soc. A: Math. Phys. Eng. Sci. 460 (2004) 3547–3568, https://doi.org/10.1098/rspa.2004.1339.

[12] E.J. Brookes, P. Greenwood, G. Xing, The Plastic Deformation and Strain-induced Fracture of Natural and Synthetic Diamond. www.elsevier.com/locate/diamond, 1999.

[13] F.M. Van Bouwelen, W.J.P. Van Enckevort, A Simple Model to Describe the Anisotropy of Diamond Polishing, 1999.

[14] L. Pastewka, S. Moser, P. Gumbsch, M. Moseler, Anisotropic mechanical amorphization drives wear in diamond, Nat. Mater. 10 (2011) 34–38, https://doi.org/10.1038/nmat2902.

[15] W.J. Zong, X. Cheng, J.J. Zhang, Atomistic origins of material removal rate anisotropy in mechanical polishing of diamond crystal, Carbon N Y 99 (2016) 186–194, https://doi.org/10.1016/j.carbon.2015.12.001.

[16] T. Kuwahara, G. Moras, M. Moseler, Role of oxygen functional groups in the friction of water-lubricated low-index diamond surfaces, Phys. Rev. Mater. 2 (2018), https://doi.org/10.1103/PhysRevMaterials.2.073606.

[17] H. Luo, K.M. Ajmal, W. Liu, K. Yamamura, H. Deng, Polishing and planarization of single crystal diamonds: state-of-the-art and perspectives, Int. J. Extreme Manuf. 3 (2021), https://doi.org/10.1088/2631-7990/abe915.

[18] M.L. Hicks, A.C. Pakpour-Tabrizi, R.B. Jackman, Polishing, preparation and patterning of diamond for device applications, Diam. Relat. Mater. 97 (2019) 10424, https://doi.org/10.1016/j.diamond.2019.05.010.

[19] I. Friel, S.L. Clewes, H.K. Dhillon, N. Perkins, D.J. Twitchen, G.A. Scarsbrook, Control of surface and bulk crystalline quality in single crystal diamond grown by chemical vapour deposition, Diam. Relat. Mater. 18 (2009) 808–815, https://doi.org/10.1016/j.diamond.2009.01.013.

[20] Y. Chen, L. Zhang, Polishing of Diamond Materials, Springer London, London, 2013, https://doi.org/10.1007/978-1-84996-408-1.

[21] Y. Chen, L. Zhang, Polishing of Diamond Materials, 2016.

[22] A.B. Muchnikov, A.L. Vikharev, J.E. Butler, V.V. Chernov, V.A. Isaev, S.A. Bogdanov, A.I. Okhapkin, P.A. Yunin, Y.N. Drozdov, Homoepitaxial growth of CVD diamond after ICP pretreatment, Phys. Status Solidi A Appl. Mater. Sci. 212 (2015) 2572–2577, https://doi.org/10.1002/pssa.201532171.

[23] B.R. Lawn, Indentation of ceramics with spheres: a century after Hertz, J. Am. Ceram. Soc. 81 (1998) 1977–1994.

[24] B.R. Lawn, Hertzian fracture in single crystals with the diamond structure, J. Appl. Phys. 39 (1968) 4828–4836, https://doi.org/10.1063/1.1655847.

[25] B.R. Lawn, H. Komatsu, The nature of deformation around pressure cracks on diamond, Philos. Mag. 14 (1966) 689–699, https://doi.org/10.1080/14786436608211965.

[26] J.E. Field, The mechanical and strength properties of diamond, Rep. Prog. Phys. 75 (2012) 126505, https://doi.org/10.1088/0034-4885/75/12/126505.

[27] J.G. Bell, M.E.C. Stuivinga, A.G. Thornton, J. Wilks, The Cracking and Fatigue of Diamond. http://iopscience.iop.org/0022-3727/10/10/014, 1977.

[28] B. Lawn, R. Wilshaw, Review indentation fracture: principles and applications, J. Mater. Sci. 10 (1975) 1049–1081.

[29] Y. Enomoto, Sliding fracture of soda-lime glass in liquid environments, J. Mater. Sci. 16 (1981) 3365–3370.

[30] M. Casey, J. Wilks, Cathodoluminescence in deformed diamond, Nature 239 (1972) 393–394.

[31] J.E. Field, C.S.J. Pickles, Strength, fracture and friction properties of diamond, Diam. Relat. Mater. 5 (1996) 625.

[32] T. Zhu, J. Li, S. Yip, Atomistic configurations and energetics of crack extension in silicon, Phys. Rev. Lett. 93 (2004) 205504, https://doi.org/10.1103/PhysRevLett.93.205504.

[33] J. Kermode, J. Greisser, L. Pastewka, W.G. Nöhring, M. Aldegunde, J. Brixey, A. Gola, J. Golebiowski, P. Grigorev, J. Hoermann, R. Jana, T. Junge, A. Klemenz, H. Lambert, J. Oldenstaedt, P. Patel, T. Reichenbach, L. Frérot, Z. Zheng, MatSciPy 9 (93) (2023) 5668, https://doi.org/10.21105/joss.05668.

[34] M. Qamar, M. Mrovec, Y. Lysogorskiy, A. Bochkarev, R. Drautz, Atomic cluster expansion for quantum-accurate large-scale simulations of carbon, J. Chem. Theory Comput. (2023), https://doi.org/10.1021/acs.jctc.2c01149.

[35] H. Kawarada, Hydrogen-terminated diamond surfaces and interfaces, Surf. Sci. Rep. 26 (1996) 205–259.

[36] B.P. Reed, M.E. Bathen, J.W.R. Ash, C.J. Meara, A.A. Zakharov, J.P. Goss, J.W. Wells, D.A. Evans, S.P. Cooil, Diamond (111) surface reconstruction and epitaxial graphene interface, Phys. Rev. B 105 (2022) 205304, https://doi.org/10.1103/PhysRevB.105.205304.

[37] B.R. Lawn, S.M. Wlederhorn, D.E. Roberts, Effect of sliding friction forces on the strength of brittle materials, J. Mater. Sci. 19 (1984) 2561–2569.

[38] J.R. Kermode, A. Gleizer, G. Kovel, L. Pastewka, G. Csányi, D. Sherman, A. De Vita, Low speed crack propagation via kink formation and advance on the silicon (110) cleavage plane, Phys. Rev. Lett. 115 (2015) 135501, https://doi.org/10.1103/PhysRevLett.115.135501.

[39] G. Kern, J. Hafner, J. Furthmuer, G. Kresse, Surface Reconstruction and Electronic Properties of Clean and Hydrogenated Diamond (111) Surfaces, 1996.

[40] M. De La Pierre, M. Bruno, C. Manfredotti, F. Nestola, M. Prencipe, C. Manfredotti, The (100), (111) and (110) surfaces of diamond: an ab initio B3LYP study, Mol. Phys. 112 (2014) 1030–1039, https://doi.org/10.1080/00268976.2013.829250.

[41] B.J. Waclawski, D.T. Pierce, N. Swanson, R.J. Celotta, Direct verification of hydrogen termination of the semiconducting diamond (111) surface, J. Vac. Sci. Technol. V 21 (1982) 368–370, https://doi.org/10.1116/1.571782.

[42] S.-T. Lee, G. Apai, Surface phonons and CH vibrational modes of diamond (100) and (111) surfaces, Phys. Rev. B 48 (1993) 2684–2689.

[43] R.P. Chin, J.Y. Huang, Y.R. Shen, T.J. Chuang, H. Seki, Interaction of Atomic Hydrogen With the Diamond C(111)surface Studied by Infrared-Visible Sum-Frequency-Generation Spectroscopy, 1995.

[44] G. Kern, J. Hafner, G. Kresse, Atomic and electronic structure of diamond (111) surfaces II. (2 x 1) and sqrt(3) x sqrt(3) reconstructions of the clean and hydrogen-covered three dangling-bond surfaces, Surf. Sci. 366 (1996) 464–482.

[45] Y. Yue, Y. Gao, W. Hu, B. Xu, J. Wang, X. Zhang, Q. Zhang, Y. Wang, B. Ge, Z. Yang, Z. Li, P. Ying, X. Liu, D. Yu, B. Wei, Z. Wang, X.F. Zhou, L. Guo, Y. Tian, Hierarchically structured diamond composite with exceptional toughness, Nature 582 (2020) 370–374, https://doi.org/10.1038/s41586-020-2361-2.

[46] C. Cayron, Diffraction artefacts from twins and stacking faults, and the mirage of hexagonal, polytypes or other superstructures, Scr. Mater. 194 (2021) 113629, https://doi.org/10.1016/j.scriptamat.2020.11.014.

[47] Y. Zeng, Q. Zhang, Y. Wang, J. Jiang, H. Xing, X. Li, Toughening and crack healing mechanisms in nanotwinned diamond composites with various polytypes, Phys. Rev. Lett. 127 (2021) 066101, https://doi.org/10.1103/PhysRevLett.127.066101.

[48] K. Qiu, J. Hou, S. Chen, X. Li, Y. Yue, B. Xu, Q. Hu, L. Liu, Z. Yang, A. Nie, Y. Gao, T. Jin, J. Wang, Y. Li, Y. Wang, Y. Tian, L. Guo, Self-healing of fractured diamond, Nat. Mater. 22 (2023) 1317–1323, https://doi.org/10.1038/s41563-023-01656-4.

[49] T.M. Moses, J.E. Shigley, S.F. McClure, J.I. Koivula, M. Van Daele, Observations on GE-processed diamonds: a photographic record, Gems Gemol. (1999) 14–22.

[50] Y. Wang, H.J. Joyce, Q. Gao, X. Liao, H.H. Tan, J. Zou, S.P. Ringer, Z. Shan, C. Jagadish, Self-healing of fractured GaAs nanowires, Nano Lett. 11 (2011) 1546–1549, https://doi.org/10.1021/nl104330h.

[51] B.R. Lawn, Diffusion-controlled Subcritical Crack Growth in the Presence of a Dilute Gas Environment, 1974.